Particles II

Access the latest eBook →

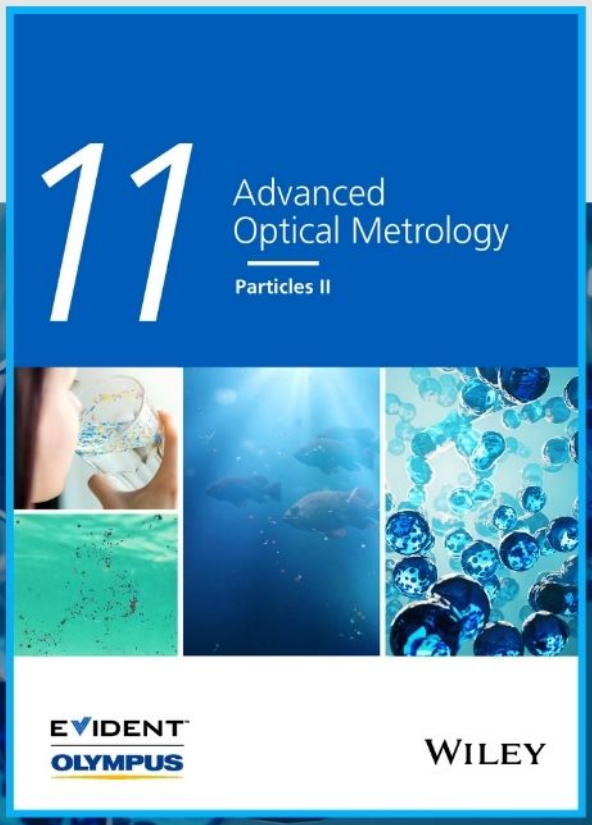

Impact on Biological Systems and the Environment

This eBook is dedicated to the research of Professor David Wertheim.
In collaboration with various groups, Professor Wertheim uses confocal microscopy to analyse the impact of different types of particles on human health and the environment, with a focus on human health-hazardous particles detected with solid-state nuclear track detectors (SSNTD). Download for free, today.

EVIDENT
OLYMPUS

WILEY

small methods
www.small-methods.com

Metal–Organic Framework Derived Fe_7S_8 Nanoparticles Embedded in Heteroatom-Doped Carbon with Lithium and Sodium Storage Capability

Huihua Li, Yuan Ma, Huang Zhang, Thomas Diemant, R. Jürgen Behm, Alberto Varzi, and Stefano Passerini**

Iron sulfides are promising materials for lithium- and sodium-ion batteries owing to their high theoretical capacity and widespread abundance. Herein, the performance of an iron sulfide-carbon composite, synthesized from a Fe-based metal–organic framework (Fe-MIL-88NH$_2$) is reported. The material is composed of ultrafine Fe_7S_8 nanoparticles (<10 nm in diameter) embedded in a heteroatom (N, S, and O)-doped carbonaceous framework (Fe_7S_8@HD-C), and is obtained via a simple and efficient one-step sulfidation process. The Fe_7S_8@HD-C composite, investigated in diethylene glycol dimethyl ether-based electrolytes as anode material for lithium and sodium batteries, shows high reversible capacities (930 mAh g^{-1} for lithium and 675 mAh g^{-1} for sodium at 0.1 A g^{-1}). In situ X-ray diffraction reveals an insertion reaction to occur in the first lithiation and sodiation steps, followed by conversion reactions. The composite electrodes show rather promising long-term cycling stability and rate capability for sodium storage in glyme electrolyte, while an improved rate capacity and long-term cycling stability (800 mAh g^{-1} after 300 cycles at 1 A g^{-1}) for lithium can be achieved using conventional carbonates.

1. Introduction

Over the past decades, the rising demand for sustainable energies has driven the development of highly efficient energy storage systems.[1] Lithium-ion batteries (LIBs) are among the most common electrochemical energy storage devices, being widely used for powering portable electronics and electric vehicles, thanks to their high energy and power density.[2] In view of the limited raw materials supply, however, sodium-ion batteries (SIBs) are attracting increasing interest due to the widespread abundance of sodium (i.e., potentially lower cost), while sharing the operating principles with LIBs.[3] In this respect, SIBs are attracting special attention for large-scale energy storage devices.[4] The energy density of both LIBs and SIBs is limited by the volumetric capacity of the negative electrode (usually referred to as anode) material. This is especially true for SIBs, due to the lower specific capacity of, for example, hard carbon with respect to graphite.[5] Therefore, the development of high-performance anode materials with long cycle life and high reversible capacity is a major task for the development of next-generation LIBs and SIBs.

Given the similar battery chemistries, various carbon-based materials,[6] alloy-type materials,[2a] and transition-metal oxides/sulfides[7] have been extensively investigated for both LIBs and SIBs. Among these anode materials, transition-metal sulfides (TMSs, e.g., MnS, FeS_2, MoS_2, CuS, SnS_2, and Fe_7S_8) with a conversion reaction mechanism exhibit highly reversible capacities and intrinsic safety for lithium and sodium storage.[8] Compared to their metal oxide counterparts, TMSs usually show faster reaction kinetics owing to their higher electronic conductivity and their better mechanical integrity, resulting from the smaller volumetric change.[5a,8a] Among the various reported TMSs, iron sulfides have been recognized as one of the most promising alternative due to their cost-effectiveness, high theoretical capacity (FeS: 609 mAh g^{-1}, FeS_2: 894 mAh g^{-1}), abundance, and low toxicity.[6] Unfortunately, their practical application is still hindered by limited conversion rates and mechanical instability upon extended cycling. To address these issues, different strategies of rational structure design have been developed, including nano/microstructure engineering and decoration with conductive carbonaceous materials. For example, Shi et al. synthesized core-shell iron sulfides-carbon nanobiscuits using a hydrothermal method.[9] The as-obtained material showed high reversible capacities of 547 mAh g^{-1} after 600 cycles for lithium and 531 mAh g^{-1} after 1 000 cycles for

H. Li, Dr. Y. Ma, Prof. H. Zhang, Dr. T. Diemant, Prof. R. J. Behm, Dr. A. Varzi, Prof. S. Passerini
Helmholtz Institute Ulm (HIU)
Helmholtzstrasse 11, Ulm D-89081, Germany
E-mail: alberto.varzi@kit.edu; stefano.passerini@kit.edu
H. Li, Dr. Y. Ma, Prof. H. Zhang, Dr. A. Varzi, Prof. S. Passerini
Karlsruhe Institute of Technology (KIT)
P.O. Box 3640, Karlsruhe D-76021, Germany
Dr. T. Diemant, Prof. R. J. Behm
Institute of Surface Chemistry and Catalysis
Ulm University
Albert-Einstein-Allee 47, Ulm D-89081, Germany
The ORCID identification number(s) for the author(s) of this article can be found under https://doi.org/10.1002/smtd.202000637.

DOI: 10.1002/smtd.202000637

sodium storage. Moreover, Huang et al. developed a 3D porous composite composed of cobalt-doped iron sulfide hollow polyhedrons embedded in a reduced graphene oxide matrix via an etching/ion-exchange strategy, which exhibited an impressive sodium storage performance with a high specific capacity of 662 mAh g^{-1} at 100 mA g^{-1}.[8a] On the other hand, heteroatom-doped (such as S-, N-, and/or O-doped) carbon matrices/layers can offer an efficient strategy to further improve the electrochemical performance of TMSs, by creating additional active sites and improving the electronic conductivity.[10] Specifically, He et al. incorporated iron sulfide nanoparticles into N-doped graphene nanosheets, which achieved a high reversible capacity of 393 mAh g^{-1} over 500 cycles under 400 mA g^{-1} for sodium.[11] Despite such promising results, there is still a need for further improvement of the iron sulfide-based materials for practical application, in particular with regards to the materials synthesis methods for easy production without performance compromises.

Metal–organic frameworks (MOFs) are a novel class of highly ordered porous materials, based on the coordination of inorganic metal ions/clusters and organic ligands.[12] MOFs feature large surface area, ultrahigh porosity, and abundant active sites, making them a suitable substrate for various applications, like drug delivery,[13] gas adsorption and separation,[14] or molecular sensing.[15] In energy storage,[16] several literature reports demonstrated that MOFs are ideal template precursors for the synthesis of composites materials consisting of porous carbon and metal or metal sulfide/oxide particles[17] because they can inherit the morphology of their parent compounds.[18] The carbon matrix generated during thermal treatment of MOFs in inert atmosphere acts as an electrically conductive path toward the electroactive particles, which, in turn, thanks to their nanosize, efficiently improve the structural stability of the anode and facilitate the diffusion of ion/electrons. Therefore, MOF-derived materials are particularly promising for high power battery applications.[19] Among the possible candidates, Fe-MOFs have been widely investigated as precursor for the synthesis of composites including iron sulfides, oxides, and selenides. For example, uniform peapod-like Fe_7Se_8@C nanorods were synthesized by selenidation of hydrothermally prepared Fe-MOFs.[19] The composites showed an outstanding rate performance for sodium storage with a high specific capacity of 218 mAh g^{-1} after 500 cycles at 3 A g^{-1}. Similarly, Cho and co-workers reported a spindle-like porous α-Fe_2O_3 material obtained by employing Fe-MOFs (Fe-MIL-88) as parental compound, which showed superior Li storage performance.[7a] Despite these interesting reports, facile synthesis methods to fabricate such high-performance iron-based electrode materials from Fe-MOF precursors, which are applicable for both Li and Na storage, are still missing.

In this work, we report the efficient and simple synthesis of spindle-like Fe_7S_8 nanoparticles embedded in heteroatom(N, S, and O)-doped porous carbonaceous frameworks (Fe_7S_8@HD-C), starting from a Fe-based MOF (denoted as Fe-MIL-88NH_2) precursor. The Fe-MIL-88NH_2 parental compound is synthesized with iron (III) nitrate nonahydrate ($Fe(NO_3)_3 \cdot 9H_2O$), 2-aminoterephthalic acid (NH_2BDC), and polyvinylpyrrolidone (PVP) in a mixture of *N,N*-dimethylformamide (DMF) and ethanol as solvent via a reflux condensation method. The resulting product is successfully transformed into Fe_7S_8@HD-C via a one-step sulfidation process. When used as Li and Na storage material, the Fe_7S_8@HD-C composite shows excellent electrochemical performance with high reversible capacities, superior rate capabilities, and long cycling stability. In addition, the reaction mechanism and structural evolution are investigated by means of in situ X-ray diffraction (XRD), revealing that intercalation takes place during the initial Li/Na uptake, before the conversion process.

2. Results and Discussion

2.1. Material Synthesis and Characterization

The synthesis of the spindle-like Fe_7S_8@HD-C nanohybrids is illustrated in **Scheme 1**. As described above, the Fe-MIL-88NH_2 precursor was prepared by a facile reflux condensation method with $Fe(NO_3)_3 \cdot 9H_2O$, NH_2BDC and PVP in a solvent mixture of DMF and ethanol. The final product Fe_7S_8@HD-C was then obtained via a simple one-step sulfidation. It is constituted by iron sulfide nanoparticles uniformly embedded in a carbonaceous framework, which forms upon carbonization of the organic ligands of the MOF.

The crystal structures of Fe-MIL-88NH_2 and Fe_7S_8@HD-C were examined by XRD. The XRD pattern of the synthesized Fe-MIL-88NH_2 in Figure S1, Supporting Information confirms the typical crystalline structure of Fe-MIL-88.[14a,20] The XRD pattern of the Fe_7S_8@HD-C composite is displayed in **Figure 1**. The reflections can be assigned to the standard Fe_7S_8 hexagonal phase structure (JCPDS NO. 24-0220), in which the four main peaks at 30.0°, 34.0°, 44.0°, and 53.3° reflect the (200), (203), (206), and (220) planes, respectively. No obvious impurity

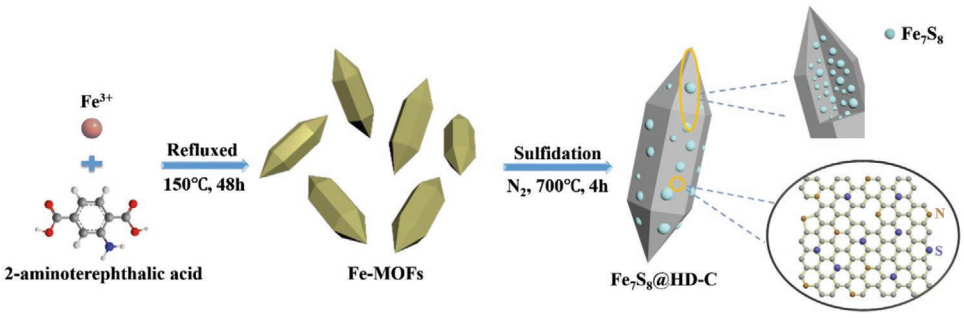

Scheme 1. Schematic illustration of the synthesis procedure for the Fe-MIL-88NH_2 precursor and the resulting product, that is, Fe_7S_8@HD-C composites.

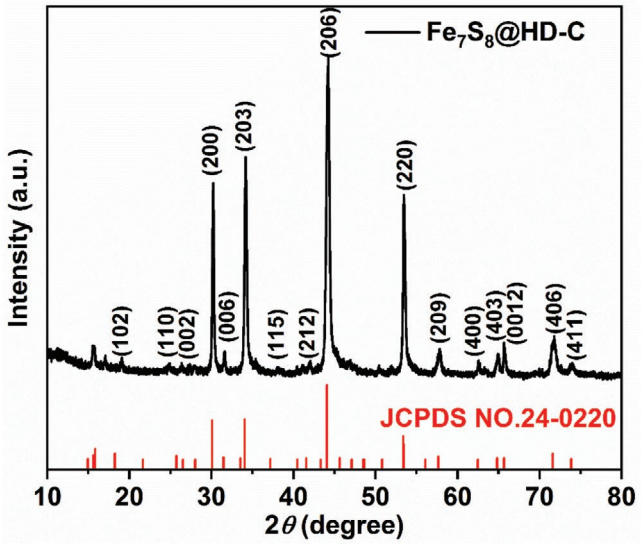

Figure 1. Powder XRD pattern of Fe_7S_8@HD-C.

phases could be detected. The nature of the carbon component in Fe_7S_8@HD-C was characterized by Raman spectroscopy (Figure S2, Supporting Information). Two strong peaks located at 1 380 and 1 570 cm^{-1} are observed, which correspond to the D-band (disordered sp^3-type carbon) and G-band (graphitic sp^2-type carbon), respectively.[21] In addition, the specific surface area and pore size distribution of Fe_7S_8@HD-C were evaluated from N_2 adsorption-desorption isotherms by multipoint Brunauer–Emmett–Teller (BET) analysis. The BET results evidence the specific surface area of Fe_7S_8@HD-C being only ca. 23 m^2 g^{-1} (Figure S3a, Supporting Information). The pore size distribution does not evidence any peculiar pore structure/hierarchy (Figure S3b, Supporting Information). The moderate porosity of Fe_7S_8@HD-C is in line with other MOF-derived materials previously reported by our group.[16]

The carbon and iron sulfide content in the Fe_7S_8@HD-C composite were estimated by thermogravimetric analysis (TGA) measurements in oxygen (Figure S4a, Supporting Information). The TGA curve exhibits multiple steps upon heating from room temperature to 800 °C. The first (small) weight loss from room temperature up to between 100 and 105 °C can be attributed to the release of adsorbed species like, for example, water. This is followed by a weight increase between 130 and 320 °C, which can be assigned to the partial conversion of Fe_7S_8 to $FeSO_4$, followed by complete oxidation into Fe_2O_3 upon further temperature ramping.[22] The finding of Fe_2O_3-related reflections in the diffractogram of the powder recovered from the TGA test (Figure S4b, Supporting Information) corroborates this thermal decomposition pathway. According to this, the weight percentage of Fe_7S_8 in the composite is calculated to be about 58%. The material was also analyzed via inductively coupled plasma optical emission spectroscopy (ICP-OES), revealing a sulfur excess with respect to the Fe_7S_8 stoichiometry (Table S1, Supporting Information). This may be attributed to additional S-containing species, as later seen by X-ray photoelectron spectroscopy (XPS) analysis.

The Fe_7S_8@HD-C composite elemental composition and surface chemistry were characterized by XPS. The survey spectrum (**Figure 2**a) corroborates the presence of only the expected elements, that is, Fe, C, O, S, and N. No other elements were identified. The chemical state of the main elements was further investigated by detail spectra. The C1s detail spectrum (Figure 2b) is dominated by a peak at 284.6 eV, which is due to graphitic sp^2-C. Further peaks at 285.5 and 288.3 eV are attributed to C—O/C—S/C—N and C=O species, respectively.[23] In the N 1s region (Figure 2c), the characteristic peaks of pyridinic, pyrrolic, and graphitic N are detected at 398.3, 400.5, and 401.4 eV, respectively. A broad feature at higher binding energy (404.5 eV) can be related to oxidic N species.[24] The S 2p detail spectrum (Figure 2d) was fitted by introducing peak doublets of five S species. The first two contributions (at 161.5/162.7 and 162.7/163.9 eV) can be attributed to sulfide (S^{2-}) anions occupying fivefold and sixfold sites in non-stoichiometric Fe_7S_8.[25] The third doublet at 163.8/165.0 eV is assigned to S atoms in the heteroatom-doped carbonaceous framework (C—S—C). The two other doublets at higher binding energy both originate from oxidized S species (166.0/167.2 eV SO_x ($x < 4$) and 168.2/169.4 eV SO_4).[6,22] The O 1s detail spectrum (Figure 2e) reveals the presence of three peaks, which are mainly ascribed to O—Fe (530.0 eV), O=C (531.3 eV) and O—C (532.9) moieties.[26] It may be noted that the SO_x/SO_4 species, which are visible in the S 2p spectra, may contribute to the O=C peak too. Finally, the Fe 2p detail spectrum (Figure 2f) is dominated by two broad peaks at ≈711.0 ($2p_{3/2}$) and 724.0 eV ($2p_{1/2}$), which are due to oxidized Fe atoms. It is difficult to discriminate between Fe^{2+} and Fe^{3+} species in XPS measurements, since both have a similar chemical shift.[27] In addition, a much smaller peak doublet located at 707.0/720.1 eV corresponds to metallic Fe, which may result from the partial reduction of Fe^{2+} during the sulfidation process at high temperature. Taken together, the XRD and XPS results confirm the presence of Fe_7S_8 and of heteroatom (N, S, and O)-doped carbonaceous frameworks, indicating the successful synthesis of the targeted nanocomposite via the one-step sulfidation of Fe-MIL-88NH_2.

The morphology of Fe-MIL-88NH_2 and Fe_7S_8@HD-C was also investigated by scanning electron microscopy (SEM) and transmission electron microscopy (TEM). The precursor particles show a uniform spindle-like structure with an average diameter/length of 185.0/485.0 nm (**Figure 3**a,b). The overall morphology is almost maintained after sulfidation with a slight shrinkage in particle size, as shown in Figure 3c. The surface of the particle becomes very rough, however. The micro-nano structure of Fe_7S_8@HD-C was further characterized by high-resolution transmission electron microscopy (HR-TEM). The iron sulfide nanoparticles have in average a particle size of ca. 10 nm and are homogeneously embedded in the carbon matrix, constituting the spindle-like composite, as illustrated in Figure 3d,e. The lattice fringes are around 0.26 nm, which matches well with the d-spacing of the (203) planes of pyrrhotite Fe_7S_8 (Figure 3f). The elemental mapping result of Fe_7S_8@HD-C (Figure 3g) demonstrates the presence of Fe and S in the spindle-like carbonaceous frameworks. In addition, the uniform distribution of N, S, and O within the spindle-like nanocomposites indicates homogenous distribution of the heteroatom-doped carbon.

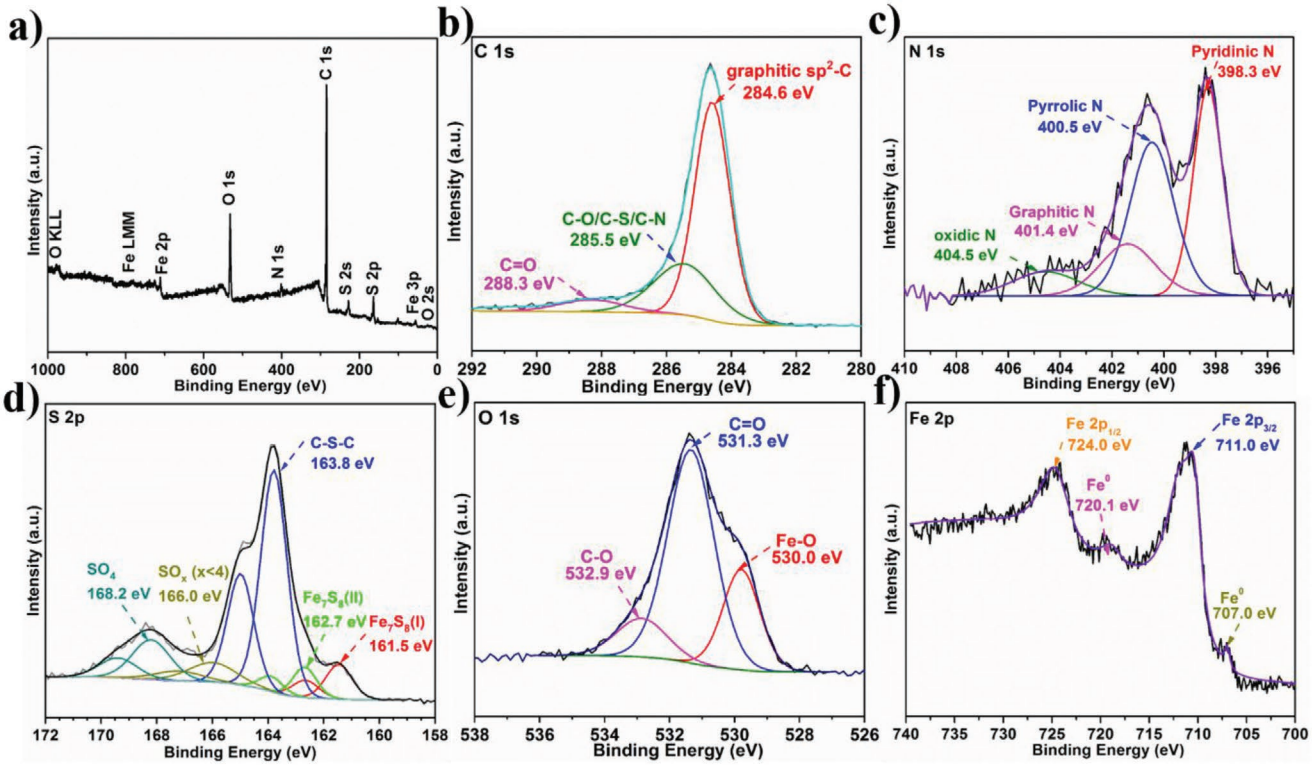

Figure 2. XPS spectra of the as-obtained Fe_7S_8@HD-C powder. a) Survey spectrum and high-resolution detail spectra in the b) C 1s, c) N 1s, d) S 2p, e) O 1s, and f) Fe 2p region.

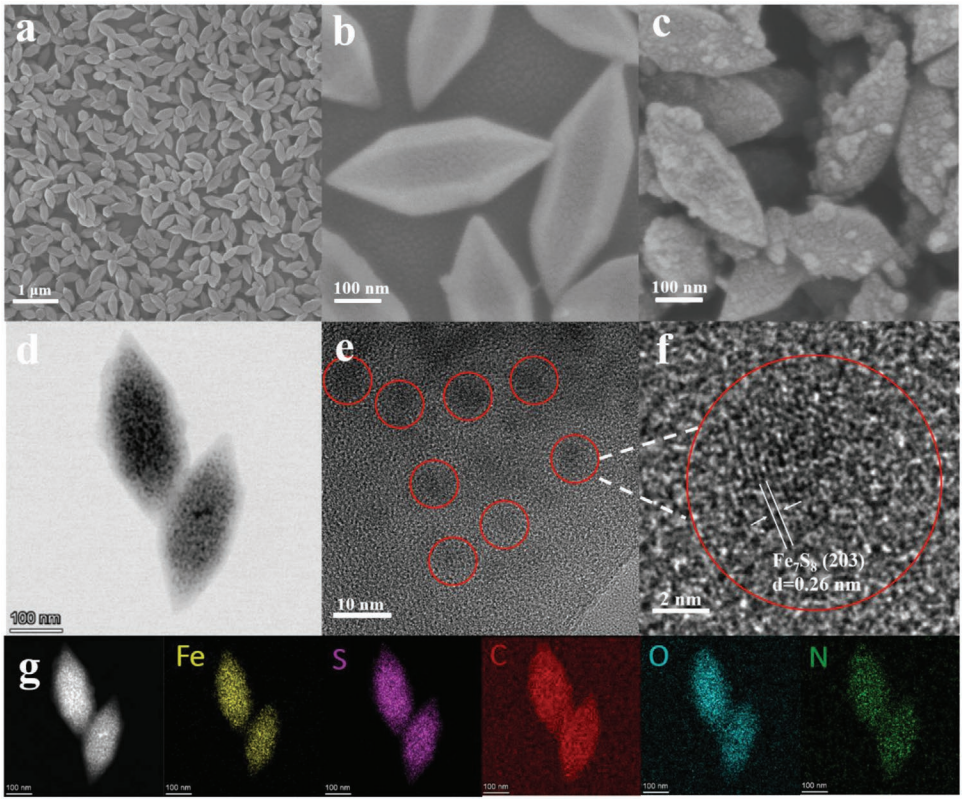

Figure 3. Morphological and structural features of the Fe-MIL-88NH_2 precursor and the Fe_7S_8@HD-C composite. SEM images of a,b) Fe-MIL-88NH_2 and c) Fe_7S_8@HD-C. d–f) HR-TEM images of Fe_7S_8@HD-C with different magnification. g) Elemental mapping images of Fe_7S_8@HD-C.

2.2. Lithium versus Sodium: The Storage Mechanism

Diethylene glycol dimethyl ether (DEGDME)-based electrolytes have been reported to be compatible with transition metal oxides and sulfides, providing high cycling stability and reversibility.[28] Thus, the Fe_7S_8@HD-C composites were first investigated in DEGDME electrolytes for both sodium and lithium storage. While $NaPF_6$ was used as salt to investigate the sodium storage, due to the limited solubility of $LiPF_6$ in DEGDME, LiFSI was used in the case of lithium.

2.2.1. Lithium Storage Mechanism

Figure 4a shows the initial four cyclic voltammetry (CV) curves at a scan rate of 0.05 mV s^{-1} in LIB half cells in the potential range from 0.01 to 3.0 V. The CV curves show multiple features, some of which disappear after the first cycle, clearly evidencing a substantial transformation of the material upon consecutive lithiation–delithiation cycles. Galvanostatic charge–discharge (GCD) voltage profiles of Fe_7S_8@HD-C half-cells were also recorded at 0.1 A g^{-1} in the voltage range of 0.01 to 3.0 V. The first five cycles are displayed in Figure 4b. The plateaus observed in the voltage profiles correspond very well to the peaks observed in the CV. The Columbic efficiency (CE) in the first cycle is 69.3%. Afterward, the CE stabilizes at about 96% which is, however, relatively low.

To clarify the electrochemical reaction mechanism of Fe_7S_8, in situ XRD measurements were performed during the first (de)lithiation process. The XRD patterns (48 scans) and the first galvanostatic discharge and charge profile recorded simultaneously are displayed in Figure 4c,d. The first discharge profile can be divided into two regions, highlighted in the waterfall XRD panel by different colors. The XRD patterns of region 1, which ranges from OCV to 1.5 V (from scan 1 to scan 4, Figure 4d; Figure S5, Supporting Information), show that the peaks of Fe_7S_8 located at 30.0° and 33.9° gradually decrease upon lithiation. At the same time, peaks associated to Li_2FeS_2 (≈28.4° and 39.2°, JCPDS No. 36-1088) gradually evolve (Figure S5a, Supporting Information). This is attributed to the first lithiation reaction of Fe_7S_8 to form

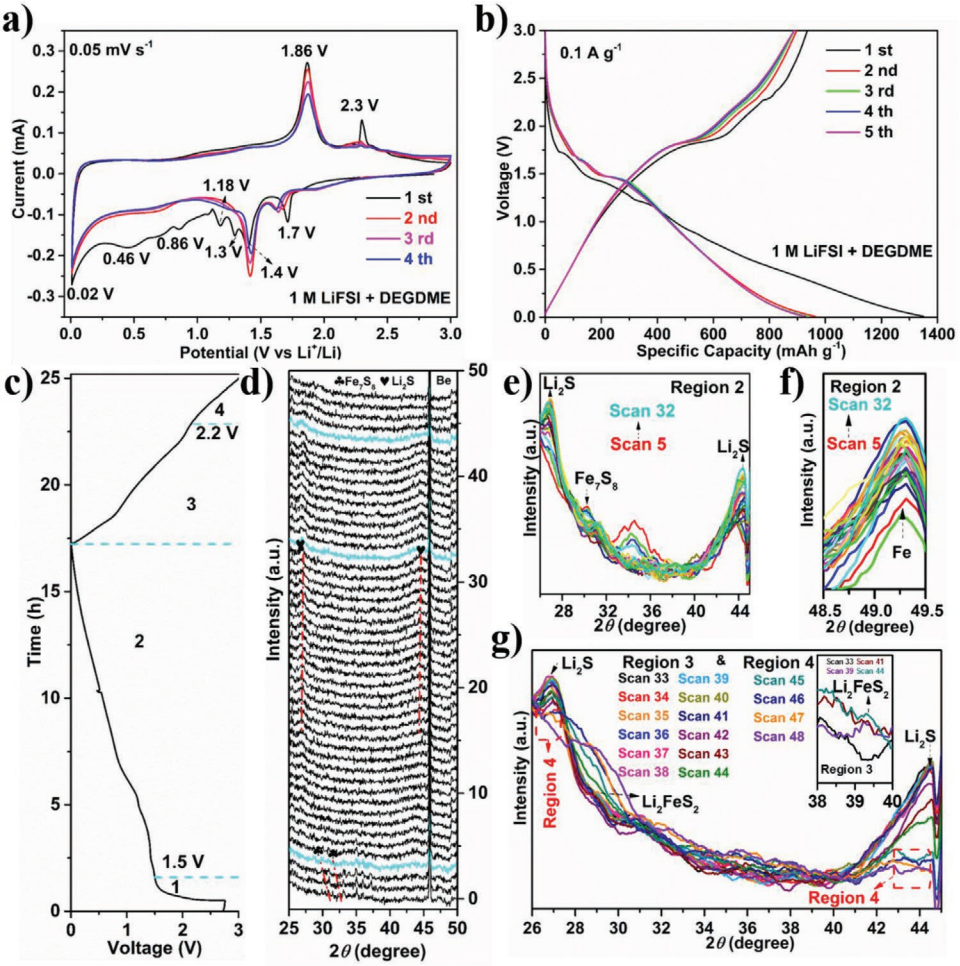

Figure 4. Lithium storage performance and mechanistic analysis of Fe_7S_8@HD-C-based electrodes in 1 M LiFSI- DEGDME. a) CV profiles of the initial 4 cycles at a scan rate of 0.05 mV s^{-1} in the potential range from 0.01 to 3.0 V. b) Voltage profiles of the initial five cycles at 0.1 A g^{-1}. c) Initial (dis-) charge profile. d) Waterfall plot of the XRD patterns recorded consecutively during (dis-)charge (scans 1–48). Selected regions of the waterfall plot: e,f) region 2: scans 5–32; g) region 3: scans 33–44 and region 4: scans 45–48.

Li_2FeS_2 (Equation 1).[29] Fe^0 is also formed to balance the reaction's stoichiometry (Figure S5b, Supporting Information). Upon deep lithiation, that is, in the second region, the reflections of Li_2S (≈27.0° and 44.8°, JCPDS: 26-1188) gradually appear (see Figure 4d,e), while the peaks of Li_2FeS_2 disappearing (Figure 4e) and those of Fe° further increasing (Figure 4f), indicating a conversion reaction between Li_2FeS_2 and Li^+ to form Li_2S and metallic iron (Equation 2).[5b] Meanwhile, the lithiation of carbon at low potential (<0.5 V) must also occur (Equation 3).[30] However, no carbon-related features could be detected in the XRD spectra, implying a poorly ordered nature of the carbonaceous framework. During the following delithiation process, in region 3 (from 0.01 to 2.2 V, scans 33–44, Figure 4g), the peaks of Li_2S become weaker and nearly disappear. At the same time, the peaks of Li_2FeS_2 gradually re-emerge, resulting from the conversion reaction between Li_2S and Fe^0 to form Li_2FeS_2 (Equation 5).[9] For the subsequent charge up to the cut-off potential of 3.0 V, that is, region 4 (from 2.2 to 3.0 V, scans 45–48), the peaks of Li_2FeS_2 completely disappear. However, the signal of Fe_7S_8 could not be observed, suggesting that the original phase is not recovered. According to the previous studies, the result can be ascribed to the formation of $Li_{2-x}FeS_2$ (Equation 6).[31,32]. Overall, the reaction mechanism can be summarized as follows:

Discharge:
Region 1

$$Fe_7S_8 + 8Li^+ + 8e^- \rightarrow 4Li_2FeS_2 + 3Fe^0 \quad (OCV - 1.5\,V, \text{Insertion / conversion}) \tag{1}$$

Region 2

$$Li_2FeS_2 + 2Li^+ + 2e^- \rightarrow 2Li_2S + Fe^0 \quad (1.5 - 0.01\,V, \text{Conversion}) \tag{2}$$

$$C_6 + xLi^+ + xe^- \rightarrow Li_xC_6 \quad (\text{Below } 0.5\,V, \text{Insertion(Carbon)}) \tag{3}$$

Charge:
Region 3

$$Li_xC_6 \rightarrow C_6 + xLi^+ + xe^- \quad (\text{Above } 0.01\,V, \text{De - insertion(Carbon)}) \tag{4}$$

$$2Li_2S + Fe^0 \rightarrow Li_2FeS_2 + 2Li^+ + 2e^- \quad (0.01 - 2.2\,V, \text{Conversion}) \tag{5}$$

Region 4

$$Li_2FeS_2 \rightarrow Li_{2-x}FeS_2 + xLi^+ + xe^- \quad (0.5 < x < 0.8, 2.2 - 3.0\,V, \text{De - insertion}) \tag{6}$$

2.2.2. Sodium Storage Mechanism

The sodium storage properties of Fe_7S_8@HD-C were also investigated in DEGDME, as illustrated in detail in **Figure 5**. Figure 5a shows the CV curves of a Fe_7S_8@HD-C electrode collected with 1 M $NaPF_6$-DEGDME, which substantially differ from those recorded upon lithiation (compare Figures 4a and 5a). Nonetheless, there is a substantial transformation of the material upon consecutive sodiation-desodiation cycles. In fact, the cathodic peaks in the second scan show a slight shift to lower potential, suggesting changes in the desodiation process after the initial (de)sodiation, which might go along with a structural reorganization after the first cycle. After the second cycle, the following CV curves exhibit no obvious peak shift, demonstrating the good reversibility of sodium uptake/release of Fe_7S_8@HD-C. GCD tests were also performed using a current density of 0.1 A g^{-1} in the potential range of 0.01–3.0 V (vs Na/Na^+). The initial discharge/charge specific capacities were 815 and 612 mAh g^{-1}, respectively, resulting in a CE of 78.4% (Figure 5b). After the first cycle, the CE rapidly approaches 100%, indicating the highly reversibility of Na storage in the Fe_7S_8@HD-C compared to Li.

In order to investigate the sodium storage mechanism and structural evolution of Fe_7S_8@HD-C composite in more detail, in situ XRD measurements during the (de)sodiation process were performed. Figure 5c shows the initial galvanostatic (dis-)charge profile, while the corresponding XRD patterns are presented in Figure 5d. The first cycle can be divided into four different regions. During the initial sodiation (region 1, from OCV to 0.95 V), the two peaks centered at 33.9° and 44.0° (Figure 5e) both shift to lower 2θ values and gradually disappear, indicating an expansion of the crystal structure as a result of Na uptake into Fe_7S_8 (Equation 7). Different from the lithiation process, the sodiation results in the formation of $Na_xFe_7S_8$, that is, the formation of Fe^0 does not occur.[5b,8a] In region 2 (from 0.95 to 0.01 V, Figure 5f), a broad peak belonging to cubic Na_2S (≈38.9°, JCPDS No. 23-0441) and a new shoulder peak of Fe^0 (≈42.6°, JCPDS No. 34-0529) appear, resulting from the conversion reaction of $Na_xFe_7S_8$ into Na_2S and metallic Fe^0 (Equation 8).[6] Additionally, the sodiation/de-sodiation of carbon at low potential cannot be excluded (Equations 9 and 10).[3a,33] Unfortunately, as in the case of Li, it could not be directly proven via in situ XRD. For the subsequent charge up to the cut-off potential of 1.31 V (referred to region 3: from 0.01 to 1.31 V, that is, the anodic peak at 1.37 V in CV), the intensities of Fe^0 and Na_2S peaks gradually decrease (Figure 5g), indicating the conversion of Na_2S and Fe^0 back to, presumably, Na_2FeS_2 (Equation 11). When the electrode is polarized further to 3 V (region 4, scans 43–53, Figure 5h), a small signal of Fe_7S_8 appears at 33.9°, coupled with the intensity decrease of the reflection related to metallic Fe. According to previous studies and the previous analysis of CV profiles, the result is attributed to the two-step conversion reaction of Na_2FeS_2 into Fe_7S_8 (Equations 12 and 13).[9,32a,34] It should be noted that Na_2FeS_2 could not be detected, suggesting a low crystallinity or an amorphous structure of the material.[8a] Meanwhile, the Na_2S could still be detected at the fully charged state, indicating that the conversion is not fully completed. In conclusion, the first-cycle (de)sodiation reaction mechanism of Fe_7S_8@HD-C can be briefly described as it follows:

Discharge:
Region 1

$$Fe_7S_8 + xNa^+ + xe^- \rightarrow Na_xFe_7S_8 \quad (OCV - 0.95\,V, \text{Insertion}) \tag{7}$$

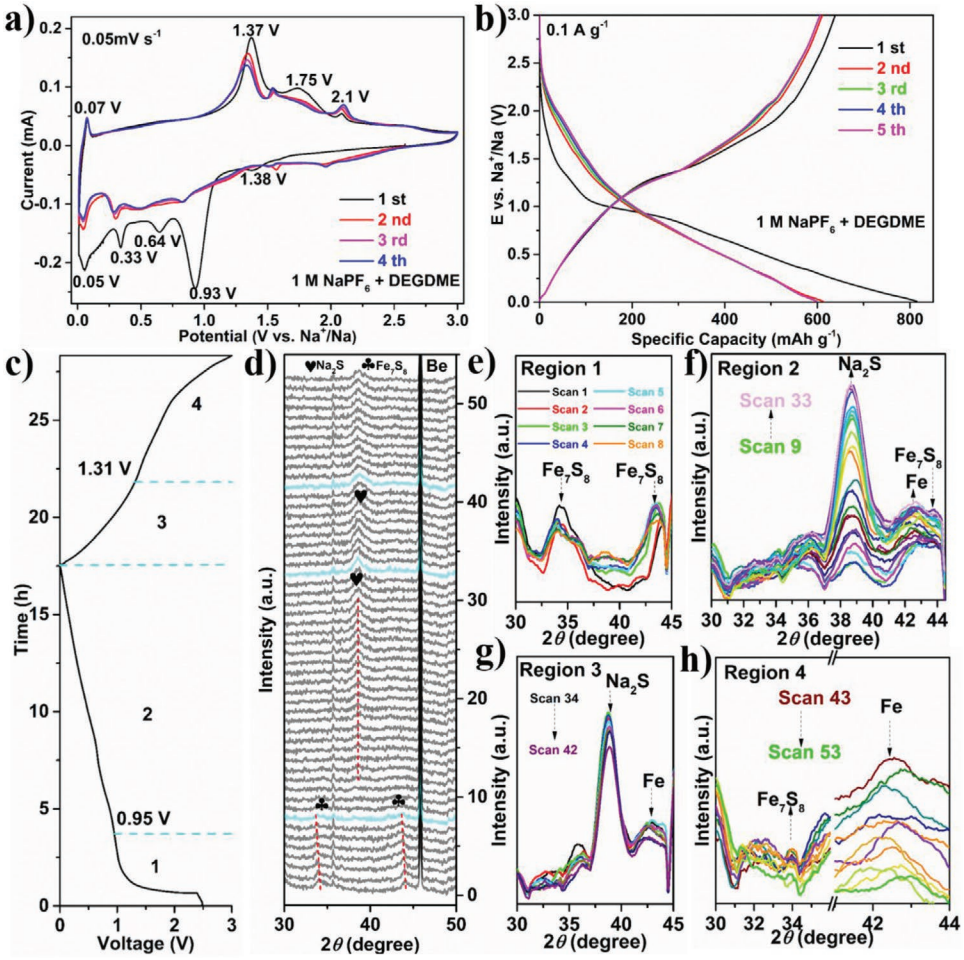

Figure 5. Sodium storage performance and mechanistic analysis of a Fe_7S_8@HD-C electrode with 1 M $NaPF_6$- DEGDME. a) CV profiles of the initial 4 cycles at a scan rate of 0.05 mV s^{-1} in the potential range from 0.01 to 3.0 V. b) Voltage profiles of the initial five cycles at 0.1 A g^{-1}. c) (Dis-) charge profile. d) The corresponding waterfall plot of the consecutively recorded XRD patterns (scans 1–53). Selected regions of the waterfall plot: e) region 1: scans 1–8; f) region 2: scans 9–33; g) region 3: scans 34–42; h) region4: 43–53.

Region 2

$$Na_xFe_7S_8 + (16-x)Na^+ + (16-x)e^- \rightarrow 8Na_2S + 7Fe^0 \quad (0.95-0.01\,V, \text{Conversion}) \tag{8}$$

$$C + xNa^+ + xe^- \rightarrow Na_xC \quad (\text{Below } 0.3\,V, \text{Insertion(Carbon)}) \tag{9}$$

Charge:
Region 3

$$Na_xC \rightarrow C + xNa^+ + xe^- \quad (\text{Below } 0.3\,V, \text{De-insertion(Carbon)}) \tag{10}$$

$$2Na_2S + Fe^0 \rightarrow Na_2FeS_2 + 2Na^+ + 2e^- \quad (0.01-1.31\,V, \text{Conversion}) \tag{11}$$

Region 4

$$Na_2FeS_2 \rightarrow Na_{2-x}FeS_2 + xNa^+ + xe^- \quad (0.5 < x < 0.8, 1.31-3.0\,V, \text{De-insertion}) \tag{12}$$

$$4Na_2FeS_2 + 3Fe^0 \rightarrow Fe_7S_8 + 8Na^+ + 8e^- \quad (1.31-3.0\,V, \text{Conversion}) \tag{13}$$

2.3. Electrochemical Performance

2.3.1. Lithium Storage Performance

First, Fe_7S_8@HD-C was investigated as negative electrode for LIBs. **Figure 6**a shows the long-term cycling stability at high current density (1 A g^{-1}) in 1 M LiFSI-DEGDME and 1 M $LiPF_6$-EC/DEC with 2 wt% VC. In DEGDME electrolyte, Fe_7S_8@HD-C shows a satisfactory cycling stability during the initial cycles. However, an obvious capacity decay is observed upon prolonged operation to 300 cycles. On the contrary, the material shows a reversible capacity of ca. 800 mAh g^{-1} without obvious capacity decay when cycled with the conventional carbonate electrolyte (1 M $LiPF_6$-EC/DEC+2 wt% VC), which was then used for the further investigation. In order to further understand the effect of electrolytes on the cycling performance, the voltage profiles (1st, 2nd, and 50th cycles) of Fe_7S_8@HD-C in both 1 M

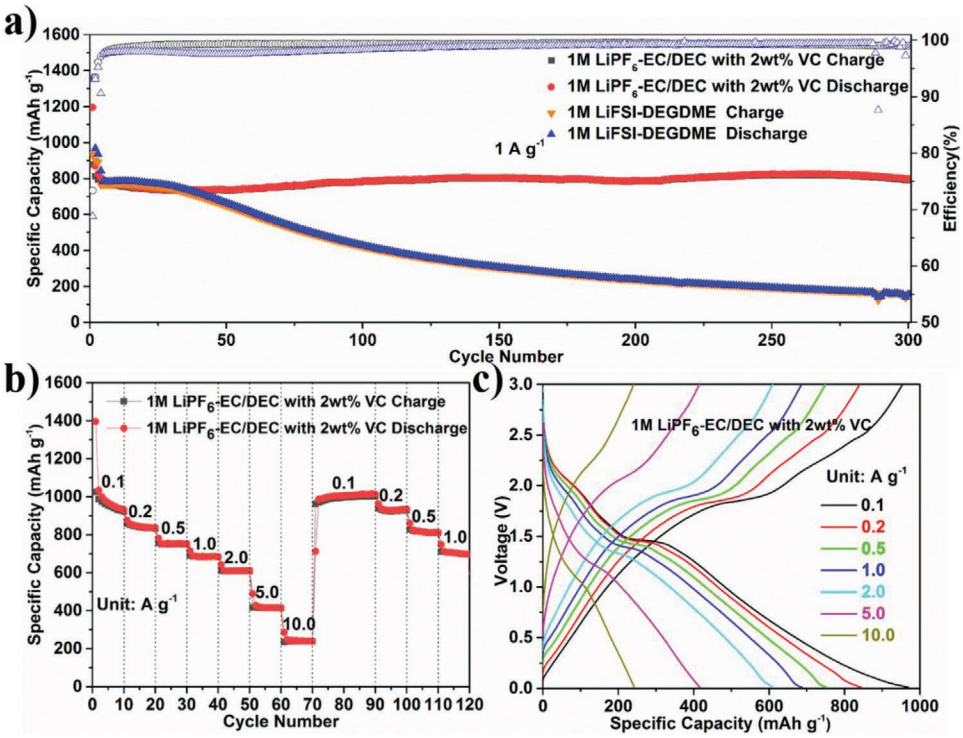

Figure 6. Lithium storage performance of Fe_7S_8@HD-C. a) Cycling performance at 1.0 A g^{-1} for 300 cycles in 1 M LiFSI-DEGDME and 1 M $LiPF_6$-EC/DEC with 2 wt% VC. b) Rate performance at various current densities in 1 M $LiPF_6$-EC/DEC with 2 wt% VC. c) Galvanostatic discharge–charge profiles at different current densities in 1 M $LiPF_6$-EC/DEC with 2 wt% VC, ranging from 0.1 to 10.0 A g^{-1} for selected cycles (i.e., the 5th, 15th, 25th, 35th, 45th, 55th, and 65th).

LiFSI-DEGDME and 1 M $LiPF_6$-EC/DEC with 2 wt% VC are plotted in Figure S6, Supporting Information. It can be clearly seen that in ether-based electrolyte the characteristic plateaus entirely disappear in the first 50 cycles, resulting in a rapid capacity fading. Although the exact reason is not known to date, the solubility of polysulfides (PS) intermediates (Li_2S_n) in the ether electrolyte may be responsible for the observed behavior. In particular, if the conversion of iron sulfide in not completely reversible, elemental sulfur may be generated upon cycling. This would then cause the formation of long chain PS that are highly soluble in ethers.[35] Despite notoriously undergoing nucleophilic attack by PS, the carbonate electrolyte displays in our case improved stability and CE, suggesting only minor dissolution of PS. Figure S7, Supporting Information shows the initial four CV curves at a scan rate of 0.05 mV s^{-1} between 0.01 and 3.0 V. The results demonstrate the similar electrochemical behaviors with DEGDME-based electrolyte, with intercalation and subsequent multistep conversion reaction mechanisms. To confirm the electrochemical reaction mechanism of Fe_7S_8@HD-C electrode in 1 M $LiPF_6$-EC/DEC with 2 wt% VC, in situ XRD measurements were also performed during the first lithiation process. Figure S8, Supporting Information reports the electrode has the similar first lithiation reaction mechanism in 1 M LiFSI-DEGDME and $LiPF_6$-EC/DEC with 2 wt% VC. To explore the effect of cut-off voltage on the capacity, fresh cells were also discharged/charged in the narrower voltage range of 0.01–1.5 V at 0.1 A g^{-1} in 1 M $LiPF_6$-EC/DEC with 2 wt% VC, as displayed in Figure S9, Supporting Information, however, delivering a specific capacity of only ca. 200 mAh g^{-1} mostly due to Li insertion in the carbonaceous framework. Figure S10a, Supporting Information reports the cycling performance and corresponding CE at 0.1 A g^{-1} for 100 cycles. As clearly seen, an improved reversible capacity of 1 078 mAh g^{-1} is obtained after 100 cycles. Meanwhile, the CE increases to about 99% in the first ten cycles and reaches 99.4% after 100 cycles. The initial ten GCD profiles are displayed in Figure S10b, Supporting Information. The first lithiation and delithiation specific capacities are 1 389 and 1 016 mAh g^{-1}, respectively, resulting in an initial CE of 73.1%, slightly higher than the one in DEGDME electrolyte (69.3%). After the first cycle, the subsequent profiles almost overlap each other, demonstrating an excellent reversibility of the Fe_7S_8@HD-C composite electrodes. Interestingly, the few selected GCD profiles, taken every 10 cycles out of the initial 100 cycles (Figure S10c, Supporting Information), show a slight increase of the capacity with increasing cycle number. This is explained by the activation of the electrode material after the initial cycles (incomplete de-conversion reactions) and/or the reversible formation/dissolution of polymeric gel-like species constituting the SEI.[36,37] An ex situ SEM image recorded on the electrode after 100 cycles (Figure S11, Supporting Information) demonstrates that the morphology of the Fe_7S_8@HD-C composite was still retained, indicating that the heteroatom-doped carbon framework can efficiently buffer the volume variation upon multiple (de)lithiation processes. The rate performance of Fe_7S_8@HD-C electrode was also evaluated at various current densities (Figure 6b,c). The average specific capacities obtained

are 967, 847, 756, 689, 614, 425, and 247 mAh g^{-1} at 0.1, 0.2, 0.5, 1, 2, 5, and 10 A g^{-1}, respectively. When the current density is decreased again to 0.1 A g^{-1}, the initial specific capacity value is almost entirely recovered. The lithium storage performance of the Fe_7S_8@HD-C composite is comparable and even superior to previous iron sulfides reported in the literature (see list in Table S2, Supporting Information). Actually, Fe_7S_8@HD-C shows a superior lithium storage performance in terms of rate capability and cycling stability compared with the large majority of materials reported so far.

2.3.2. Sodium Storage Performance

The sodium storage performance of Fe_7S_8@HD-C was also investigated in 1 M $NaPF_6$-DEGDME, as presented in detail in **Figure 7**. The rather stable cycling upon the initial 100 cycles at 0.1 A g^{-1} (Figure 7a) demonstrates the high performance of this electrode material. The high CE of more than 100% points to an instability of SEI formed in glyme-based electrolyte, which was commonly observed also in other previous reports.[5b,38] The rate performance of Fe_7S_8@HD-C was probed with increasing current densities from 0.1 to 10 A g^{-1} (Figure 7b,c). The material shows reversible capacities of 595, 568, 544, 517, 476, 401, and 326 mAh g^{-1} at 0.1, 0.2, 0.5, 1, 2, 5, and 10 A g^{-1}, respectively. Remarkably, a specific capacity of 586 mAh g^{-1} can be recovered when the current density is reduced back to 0.1 A g^{-1}, corroborating the high rate capability and reversibility. Furthermore, the long-term cycling stability after the rate performance test was evaluated at 1 A g^{-1} for 200 cycles, with no obvious capacity loss observable (Figure 7c). Figure 7d shows the results of an additional long-term cycling test of the Fe_7S_8@HD-C electrode at a relatively high current density of 2 A g^{-1} for 320 cycles (after 3 cycles at 0.1 A g^{-1} as

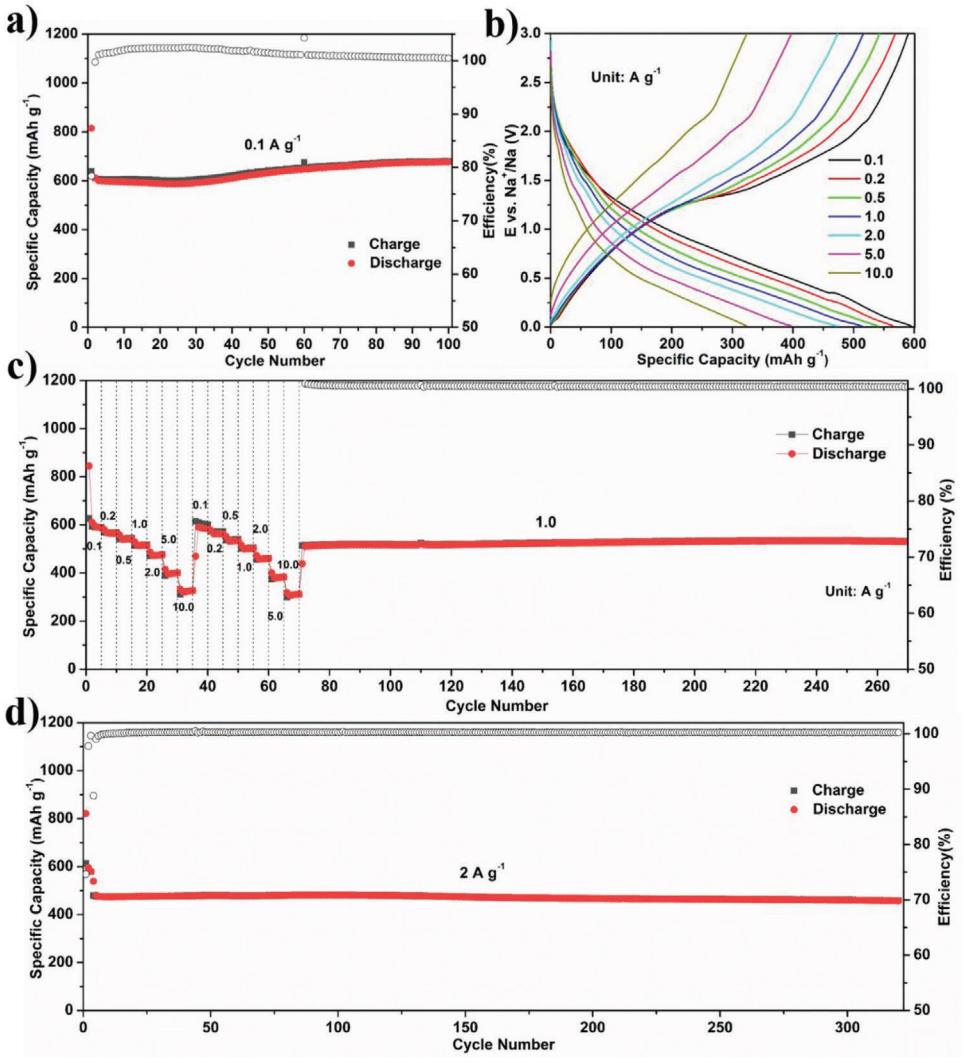

Figure 7. Sodium storage performance of Fe_7S_8@HD-C-based electrodes in three-electrode cells employing Na as reference and counter electrodes in 1 M $NaPF_6$-DEGDME. a) Cycling performance for 100 cycles at a current density at 0.1 A g^{-1}. b) Galvanostatic discharge–charge profiles at different current densities, ranging from 0.1 to 10.0 A g^{-1} for selected cycles (i.e., the 5th, 15th, 25th, 35th, 45th, 55th, and 65th). c) Rate performance at various current densities, ranging from 0.1 to 10.0 A g^{-1}. d) Cycling performance at 2 A g^{-1} for 320 cycles (after 3 cycles at 0.1 A g^{-1} in the beginning as activation step).

activation step). The electrode displays excellent cycling stability with a reversible capacity of ca. 480 mAh g^{-1} from the 5th to 320th cycle without obvious capacity decay. The cycling performance of Fe_7S_8@HD-C was also investigated in 1 M $NaPF_6$-EC/DEC with 2 wt% FEC at a current density of 2 A g^{-1} for 300 cycles, as presented in Figure S12, Supporting Information. In the carbonate electrolyte, Fe_7S_8@HD-C shows an obvious capacity decay, probably as result of the poor compatibility of the Na metal counter electrode, as evidenced in a previous paper by our group.[28a] Comparison with previous studies on similar Fe_7S_8 or Fe_7S_8-based composites evidences the outstanding electrochemical performance of Fe_7S_8@HD-C as sodium host (see Table S3, Supporting Information). To examine the mechanical integrity of the material upon (de) sodiation, the morphology evolution of the Fe_7S_8@HD-C composite in the electrode was checked by SEM after the rate performance test (Figure S13, Supporting Information). The SEM images demonstrate that the Fe_7S_8@HD-C composites retain their original structure of the active material after repeated (de)sodiation cycles, indicating that the doped carbon matrix acts as a perfect buffer. Finally, the material was also tested in the voltage range of 0.01–1.5 V at 0.1 A g^{-1}. As seen in Figure S14, Supporting Information, it initially delivers more than 300 mAh g^{-1}, which is rather promising for application in Na-ion batteries. Nevertheless, the CE needs must be improved to avoid the capacity fading observed in the first ten cycles.

3. Conclusion

Starting from the iron-based MOF of Fe-MIL-88NH_2 as precursor, we have successfully synthesized Fe_7S_8@HD-C composites via a one-step sulfidation process. The Fe_7S_8 nanoparticles are uniformly embedded in S-, N-, and O-doped carbon-based networks that can facilitate electron transport and buffer the volume changes during charge/discharge, thus enabling an excellent Li and Na storage. Specifically, Fe_7S_8@HD-C shows excellent Li-ion storage capacity of 1 078 mAh g^{-1} at 0.1 A g^{-1} after 100 cycles in carbonate electrolyte, together with an improved rate capability and a long cycling stability. Regarding Na-ion storage, the material exhibits a remarkable rate capability in DEGDME electrolyte, achieving a reversible capacity of 326 mAh g^{-1} even at rather high specific currents (i.e., 10 A g^{-1}). It also shows an excellent reversible capacity of 480 mAh g^{-1} at 2 A g^{-1} after 320 cycles. In situ XRD results revealed some interesting differences between the lithiation and sodiation mechanisms. While the first reduction follows in both cases a two-step mechanism (insertion and conversion), they differ in so far as the two processes partially overlap in the case of lithium. Additionally, upon oxidation the initial Fe_7S_8 is recovered in the case of sodium, suggesting that the de-insertion of Li may be partially irreversible. The reported results demonstrate that such a rationally designed composite, that is, iron sulfide nanoparticles incorporated in a heteroatom-doped carbon matrix, can be used in high-performance electrodes for both lithium and sodium storage. This provides a strong incentive for further research on other transition metal sulfides as active materials for rechargeable batteries.

4. Experimental Section

Chemicals: $Fe(NO_3)_3{\cdot}9H_2O$ (98.0–101.0%) was purchased from Alfa Aesar. Sulfur powder (S, 99.98%) and NH_2BDC (99%) were obtained from Sigma Aldrich Chemical Co. PVP (K30, Mw = 4 4000–5 4000) was purchased from PanReac AppliChem. Ethanol (96%) and DMF (99%) were obtained from VWR and Merck KGaA, respectively. All the chemicals were directly used as received without further purification.

Synthesis of Fe-MOF (Fe-MIL-88NH_2) Precursors: $Fe(NO_3)_3{\cdot}9H_2O$ (5 mmol, 2.02 g), NH_2BDC (5 mmol, 0.906 g), and PVP (3.5 g) were dissolved into solvent mixture (120 ml: 75 ml of DMF and 45 ml of ethanol) at room temperature under vigorous stirring to form a brown solution. Then, the solution was heated in an oil bath at 150 °C under reflux for 48 h. After cooling down to room temperature, the precipitate was collected via centrifugation and washed with distilled water and ethanol several times. Finally, the brown powder was dried at 80 °C overnight.

Synthesis of Fe_7S_8@HD-C Composites: Fe_7S_8@HD-C composites were synthesized by a one-step sulfidation process. Fe-MOF and sulfur powder (in a mass ratio of 1:5) were, respectively, put downstream and upstream of the crucible in a tube furnace, which was then heated to 700 °C (heating ramp: 5 °C min^{-1}) for 4 h under N_2 flow. After natural cooling down to room temperature, a black powder (Fe_7S_8@HD-C) was collected.

Materials Characterization: The crystal structure of Fe-MIL-88NH_2 and Fe_7S_8@HD-C was determined using XRD on a Bruker D8 Advance instrument (Cu-K_α radiation with a wavelength of 0.154 nm). In situ XRD measurements were performed in a home-made cell using a Be window as the current collector, with the potential controlled by a potentiostat/galvanostat (SP-150, BioLogic). The morphological properties of all the samples were investigated via SEM (ZEISS 1550VP). TEM and elemental mapping were carried out on a PEI Talos-F200X operated at 200 kV. Raman spectra of Fe_7S_8@HD-C were recorded using a confocal InVia Raman microspectrometer (Renishaw) using 633 nm laser radiation. The BET specific surface area of the samples was derived from the nitrogen absorption–desorption isotherms (Autosorb-iQ, Quantachrome) at 77 K. TGA was carried out under an oxygen atmosphere with a heating rate of 5 °C min^{-1} (TGA-209F, Netzsch). The Fe and S content in Fe_7S_8@HD-C were determined by ICP-OES. For this, the as-obtained Fe_7S_8@HD-C sample was dissolved in hot hydrochloric acid and investigated by means of a Spectro Arcos (Spectro Analytical Instruments) with axial plasma view. XPS spectra were recorded on a PHI 5800 Multitechnique ESCA system with monochromatized Al K_α (1 486.6 eV) radiation at a take-off angle of 45° using pass energies of 29.35 and 93.9 eV at the analyzer for detail and survey measurements, respectively. The dominant C1s peak of graphitic carbon (sp^2-C) in the carbonaceous framework was used for binding energy calibration and put to 284.6 eV. The detail spectra were analyzed by a peak fit (CasaXPS) software using a Shirley background and peaks with Gaussian/Lorentzian peak shape. For the spin-orbit splitting S 2p peak doublets, the peak ratio (2:1) and splitting (1.2 eV) were fixed, and a common FWHM was used for the $2p_{3/2}$ and $2p_{1/2}$ components of every doublet.

Electrochemical Measurements: The electrodes were prepared by casting slurries composed of Fe_7S_8@HD-C, polyvinylidene fluoride (Solef 6020, Solvay), and SuperC65 (Imerys Graphite & Carbon) in a weight ratio of 70:20:10 in *N*-methyl pyrrolidone (anhydrous, Sigma Aldrich) onto a dendritic copper foil (Schlenk, 99.9%). After the initial drying in an oven at 80 °C (3 h), disk electrodes (12 mm in diameter) were punched and further vacuum-dried for 24 h at 80 °C. The active material (Fe_7S_8@HD-C) mass loading of each disk electrode ranged between 1.2 and 1.5 mg cm^{-2}. The electrochemical tests for the characterization as lithium-ion electrode were assembled in CR2032 coin cell, using a lithium metal foil (Honjo metal) as counter electrode, 1 M $LiPF_6$ solution in a 1:1 (volume ratio) mixture of EC and diethyl carbonate (including 2 vol. % vinylene carbonate as additive) or 1 M LiFSI solution in DEGDME as electrolyte, and a glass fiber membrane disk (GF/D, Whatman) as separator. The CV of lithium storage was carried out in three-electrode Swagelok-type cells with a VMP3 potentiostat (Biologic Science Instruments) in the voltage range, that is, 0.01–3.0 V versus Li/Li^+ using a lithium metal foil (Honjo metal) as counter/reference

electrode. The sodium storage performance was tested in three-electrode Swagelok-type cells, using Na metal (Acros, 99.5%) as reference/counter electrodes, 1 M $NaPF_6$ solution in DEGDME or 1 M $NaPF_6$ solution in a 1:1 (weight ratio) mixture of EC and diethyl carbonate (including 2 wt% fluoroethylene carbonate as additive) as the electrolyte, and GF/D as separator. The CV of sodium storage was obtained in three-electrode Swagelok-type cells with a VMP3 potentiostat in the voltage range, that is, 0.01–3.0 V versus Na/Na^+. All cells were assembled in an argon-filled glovebox with H_2O and O_2 content lower than 0.1 ppm. The galvanostatic cycling tests were performed on a Maccor 3000 battery tester in the potential range between 0.01–3.0 V. All measurements were performed in climatic chambers at a constant temperature of 20 ± 1 °C.

Supporting Information

Supporting Information is available from the Wiley Online Library or from the author.

Acknowledgements

The authors thank Dr. Bingsheng Qin and Xu Liu for valuable discussions. H.L. and Y.M. gratefully acknowledge financial support from the Chinese Scholarship Council (CSC). Financial support from the Helmholtz Association Exnet pLB (SCI number 37.01.01) and the German Ministry for Education and Research (BMBF, within the M.Era-net project "NEILLSBAT," 03XP0120A) is also acknowledged. This work contributes to the research performed at CELEST (Center for Electrochemical Energy Storage Ulm-Karlsruhe).

Open access funding enabled and organized by Projekt DEAL.

Conflict of Interest

The authors declare no conflict of interest.

Authors Contributions

H.L. conceived the research idea, designed the experiments, analyzed the results, and prepared the first draft of the manuscript. Y.M. provided some information on the synthesis method of Fe-MOF and the in situ XRD test and analysis. H.Z. performed the TEM measurement and provided some help in cell fabrication and test. T.D. and R.J.B. contributed to the characterization by XPS. A.V. and S.P. supervized and coordinated the work. All authors contributed to the writing and have given approval to the final version of the manuscript.

Keywords

iron sulfide nanoparticles, lithium-ion batteries, metal–organic frameworks, porous carbonaceous frameworks, sodium-ion batteries

Received: July 25, 2020
Revised: September 3, 2020
Published online: October 26, 2020

[1] a) M. Armand, J. M. Tarascon, *Nature* **2008**, *451*, 652; b) L. Ghadbeigi, J. K. Harada, B. R. Lettiere, T. D. Sparks, *Energy Environ. Sci.* **2015**, *8*, 1640.

[2] a) D. Bresser, S. Passerini, B. Scrosati, *Energy Environ. Sci.* **2016**, *9*, 3348; b) Y. Ma, Y. Ma, D. Geiger, U. Kaiser, H. Zhang, G.-T. Kim, T. Diemant, R. J. Behm, A. Varzi, S. Passerini, *Nano Energy* **2017**, *42*, 341.

[3] a) Y. Ma, Y. Ma, D. Bresser, Y. Ji, D. Geiger, U. Kaiser, C. Streb, A. Varzi, S. Passerini, *ACS Nano* **2018**, *12*, 7220; b) B. Dunn, H. Kamath, J.-M. Tarascon, *Science* **2011**, *334*, 928; c) J. Peters, D. Buchholz, S. Passerini, M. Weil, *Energy Environ. Sci.* **2016**, *9*, 1744.

[4] M. Lee, J. Hong, J. Lopez, Y. Sun, D. Feng, K. Lim, W. C. Chueh, M. F. Toney, Y. Cui, Z. Bao, *Nat. Energy* **2017**, *2*, 861.

[5] a) L. Shen, Y. Wang, F. Wu, I. Moudrakovski, P. A. van Aken, J. Maier, Y. Yu, *Angew. Chem., Int. Ed.* **2019**, *58*, 7238; b) T. Liu, Y. Li, L. Zhao, F. Zheng, Y. Guo, Y. Li, Q. Pan, Y. Liu, J. Hu, C. Yang, *ACS Appl. Mater. Interfaces* **2019**, *11*, 19040.

[6] W. Chen, X. Zhang, L. Mi, C. Liu, J. Zhang, S. Cui, X. Feng, Y. Cao, C. Shen, *Adv. Mater.* **2019**, *31*, 1806664.

[7] a) X. Xu, R. Cao, S. Jeong, J. Cho, *Nano Lett.* **2012**, *12*, 4988; b) Z. Lu, N. Wang, Y. Zhang, P. Xue, M. Guo, B. Tang, X. Xu, W. Wang, Z. Bai, S. Dou, *ACS Appl. Energy Mater.* **2018**, *1*, 6234; c) B. Qin, H. Zhang, T. Diemant, X. Dou, D. Geiger, R. J. Behm, U. Kaiser, A. Varzi, S. Passerini, *Electrochim. Acta* **2019**, *296*, 806; d) U. Ulissi, S. Ito, S. M. Hosseini, A. Varzi, Y. Aihara, S. Passerini, *Adv. Energy Mater.* **2018**, *8*, 1801462; e) S. M. Hosseini, A. Varzi, S. Ito, Y. Aihara, S. Passerini, *Energy Storage Mater.* **2020**, *27*, 61.

[8] a) S. Huang, S. Fan, L. Xie, Q. Wu, D. Kong, Y. Wang, Y. V. Lim, M. Ding, Y. Shang, S. Chen, H. Y. Yang, *Adv. Energy Mater.* **2019**, *9*, 1901584; b) X. Y. Yu, X. W. D. Lou, *Adv. Energy Mater.* **2018**, *8*, 1701592.

[9] L. Shi, D. Li, J. Yu, H. Liu, Y. Zhao, H. Xin, Y. Lin, C. Lin, C. Li, C. Zhu, *J. Mater. Chem. A* **2018**, *6*, 7967.

[10] a) J. P. Paraknowitsch, A. Thomas, *Energy Environ. Sci.* **2013**, *6*, 2839; b) J. Yang, X. Zhou, D. Wu, X. Zhao, Z. Zhou, *Adv. Mater.* **2017**, *29*, 1604108.

[11] Q. He, K. Rui, J. Yang, Z. Wen, *ACS Appl. Mater. Interfaces* **2018**, *10*, 29476.

[12] a) S. Foley, H. Geaney, G. Bree, K. Stokes, S. Connolly, M. J. Zaworotko, K. M. Ryan, *Adv. Funct. Mater.* **2018**, *28*, 1800587; b) Q. Zhu, W. Xia, T. Akita, R. Zou, Q. Xu, *Adv. Mater.* **2016**, *28*, 6391.

[13] P. Horcajada, T. Chalati, C. Serre, B. Gillet, C. Sebrie, T. Baati, J. F. Eubank, D. Heurtaux, P. Clayette, C. Kreuz, J.-S. Chang, Y. K. Hwang, V. Marsaud, P.-N. Bories, L. Cynober, S. Gil, G. Férey, P. Couvreur, R. Gref, *Nat. Mater.* **2010**, *9*, 172.

[14] a) D. A. Reed, D. J. Xiao, M. I. Gonzalez, L. E. Darago, Z. R. Herm, F. Grandjean, J. R. Long, *J. Am. Chem. Soc.* **2016**, *138*, 5594; b) H. Wang, X. Yuan, Y. Wu, G. Zeng, H. Dong, X. Chen, L. Leng, Z. Wu, L. Peng, *Appl. Catal., B* **2016**, *186*, 19.

[15] S. Xie, J. Ye, Y. Yuan, Y. Chai, R. Yuan, *Nanoscale* **2015**, *7*, 18232.

[16] Y. Ma, Y. Ma, G. T. Kim, T. Diemant, R. J. Behm, D. Geiger, U. Kaiser, A. Varzi, S. Passerini, *Adv. Energy Mater.* **2019**, *9*, 1902077.

[17] H. Pang, W. Sun, L.-P. Lv, F. Jin, Y. Wang, *J. Mater. Chem. A* **2016**, *4*, 19179.

[18] a) R. Wu, D. P. Wang, V. Kumar, K. Zhou, A. W. Law, P. S. Lee, J. Lou, Z. Chen, *Chem. Commun.* **2015**, *51*, 3109; b) H. Li, M. Liang, W. Sun, Y. Wang, *Adv. Funct. Mater.* **2016**, *26*, 1098.

[19] X. Xu, J. Liu, J. Liu, L. Ouyang, R. Hu, H. Wang, L. Yang, M. Zhu, *Adv. Funct. Mater.* **2018**, *28*, 1707573.

[20] M. H. Pham, G. T. Vuong, A. T. Vu, T. O. Do, *Langmuir* **2011**, *27*, 15261.

[21] M.-J. Choi, J. Kim, J.-K. Yoo, S. Yim, J. Jeon, Y. S. Jung, *Small* **2018**, *14*, 1702816.

[22] W. Huang, S. Li, X. Cao, C. Hou, Z. Zhang, J. Feng, L. Ci, P. Si, Q. Chi, *ACS Sustainable Chem. Eng.* **2017**, *5*, 5039.

[23] Q. Xu, Y. Liu, C. Gao, J. Wei, H. Zhou, Y. Chen, C. Dong, T. S. Sreeprasad, N. Li, Z. Xia, *J. Mater. Chem. C* **2015**, *3*, 9885.

[24] H. Zhang, I. Hasa, B. Qin, T. Diemant, D. Buchholz, R. J. Behm, S. Passerini, *ChemElectroChem* **2017**, *4*, 1256.

[25] H. W. Nesbitt, A. G. Schaufuss, M. Scaini, G. M. Bancroft, A. R. Szargan, *Am. Mineral.* **2001**, *86*, 318.

[26] S.-J. Park, Y.-S. Jang, *J. Colloid Interface Sci.* **2001**, *237*, 91.

[27] B. Crist, *Handbook of Monochromatic XPS Spectra*, XPS International, Kawasaki **1999**.

[28] a) B. Qin, A. Schiele, Z. Jusys, A. Mariani, T. Diemant, X. Liu, T. Brezesinski, R. J. Behm, A. Varzi, S. Passerini, *ACS Appl. Mater. Interfaces* **2020**, *12*, 3697; b) K. Li, J. Zhang, D. Lin, D.-W. Wang, B. Li, W. Lv, S. Sun, Y.-B. He, F. Kang, Q.-H. Yang, L. Zhou, T.-Y. Zhang, *Nat. Commun.* **2019**, *10*, 725.
[29] B. Liu, F. Zhang, Q. Wu, J. Wang, W. Li, L. Dong, Y. Yin, *Mater. Chem. Phys.* **2015**, *151*, 60.
[30] Y. E.-E. Doron Aurbach, *J. Electrochem. Soc.* **1995**, *142*, 1746.
[31] B. Wu, H. Song, J. Zhou, X. Chen, *Chem. Commun.* **2011**, *47*, 8653.
[32] a) F. Jiang, Q. Wang, R. Du, X. Yan, Y. Zhou, *Chem. Phys. Lett.* **2018**, *706*, 273; b) X. Zhang, J. Li, J. Li, L. Han, T. Lu, X. Zhang, G. Zhu, L. Pan, *Chem. Eng. J.* **2020**, *385*, 123394.
[33] D. A. Stevens, J. R. Dahn, *J. Electrochem. Soc.* **2001**, *148*, A803.
[34] X. Wu, H. Zhao, J. Xu, Z. Zhang, W. Sheng, S. Dai, T. Xu, S. Zhang, X. Wang, Y. Wang, X. Li, *Appl. Surf. Sci.* **2019**, *492*, 504.
[35] D. Tran, H. Dong, S. Walck, S. Zhang, *RSC Adv.* **2015**, *5*, 87847.
[36] Z. Liu, F. Hu, J. Xiang, C. Yue, D. Lee, T. Song, *Part. Part. Syst. Charact.* **2018**, *35*, 1800163.
[37] a) W. Kang, Y. Tang, W. Li, X. Yang, H. Xue, Q. Yang, C.-S. Lee, *Nanoscale* **2015**, *7*, 225; b) L. Fan, W. Zhang, S. Zhu, Y. Lu, *Ind. Eng. Chem. Res.* **2017**, *56*, 2046; c) G. Zhou, D.-W. Wang, F. Li, L. Zhang, N. Li, Z.-S. Wu, L. Wen, G. Q. Lu, H.-M. Cheng, *Chem. Mater.* **2010**, *22*, 5306.
[38] D. Yang, W. Chen, X. Zhang, L. Mi, C. Liu, L. Chen, X. Guan, Y. Cao, C. Shen, *J. Mater. Chem. A* **2019**, *7*, 19709.